Integration of Rough RTP Absorbers into CIGS-Perovskite Monolithic Tandems by NiO_x(:Cu)+SAM Hole-transporting Bi-layers

Ivona Kafedjiska [a,*], Guillermo A. Farias-Basulto [b], Pablo Reyes-Figueroa [c], Tobias Bertram [d], Amran Al-Ashouri [e], Christian A. Kaufmann [f], Robert Wenisch [g], Steve Albrecht [h], Rutger Schlatmann [i], and Iver Lauermann [j]

***** Corresponding author

[a] Helmholtz-Zentrum Berlin für Materialien und Energie (HZB), Competence Centre Photovoltaics (PVcomB), Schwarzschildstraße 3, 12489, Berlin, Germany, ivona.kafedjiska@helmholtz-berlin.de

[b] Helmholtz-Zentrum Berlin für Materialien und Energie (HZB), Competence Centre Photovoltaics (PVcomB), Schwarzschildstraße 3, 12489, Berlin, Germany, guillermo.farias@helmholtz-berlin.de

[c] Helmholtz-Zentrum Berlin für Materialien und Energie (HZB), Competence Centre Photovoltaics (PVcomB), Schwarzschildstraße 3, 12489, Berlin, Germany, pablo.reyes_figueroa@helmholtz-berlin.de

[d] Helmholtz-Zentrum Berlin für Materialien und Energie (HZB), Competence Centre Photovoltaics (PVcomB), Schwarzschildstraße 3, 12489, Berlin, Germany, tobias.bertram@helmholtz-berlin.de

[e] Helmholtz-Zentrum Berlin für Materialien und Energie, Young Investigator Group Perovskite Tandem Solar Cells, Kekuléstr. 5, 12489 Berlin, Germany, amran.al-ashouri@helmholtz-berlin.de

[f] Helmholtz-Zentrum Berlin für Materialien und Energie (HZB), Competence Centre Photovoltaics (PVcomB), Schwarzschildstraße 3, 12489, Berlin, Germany, kaufmann@helmholtz-berlin.de

[g] Helmholtz-Zentrum Berlin für Materialien und Energie (HZB), Competence Centre Photovoltaics (PVcomB), Schwarzschildstraße 3, 12489, Berlin, Germany, insta-@gmx.net

[h] Helmholtz-Zentrum Berlin für Materialien und Energie, Young Investigator Group Perovskite Tandem Solar Cells, Kekuléstr. 5, 12489 Berlin, Germany, and Faculty of Electrical Engineering and Computer Science, Technical University Berlin, Germany, steve.albrecht@helmholtz-berlin.de

[i] Helmholtz-Zentrum Berlin für Materialien und Energie (HZB), Competence Centre Photovoltaics (PVcomB), Schwarzschildstraße 3, 12489, Berlin, Germany, and Faculty 1 - Energy and Information, Hochschule für Technik

und Wirtschaft Berlin, Germany,

rutger.schlatmann@helmholtz-berlin.de

[j] Helmholtz-Zentrum Berlin für Materialien und Energie (HZB), Competence Centre Photovoltaics (PVcomB), Schwarzschildstraße 3, 12489, Berlin, Germany, iver.lauermann@helmholtz-berlin.de

Abstract

We investigate the performance of monolithic copper-indium-gallium-selenide (CIGS)/perovskite tandem solar cells with two different CIGS bottom device absorbers: $Cu(In,Ga)Se_2$ or $Cu(In,Ga)(S,Se)_2$ and with three different hole-transporting layers (HTLs): NiO_x + SAM, NiO_x:Cu + SAM and SAM alone. NiO_x(:Cu) is (2 wt.% copper-doped) nickel oxide and SAM is the MeO-2PACz ([2-(3,6-dimethoxy-9H-carbazol-9-yl)ethyl]phosphonic acid) self-assembled monolayer. The CIGSe is fabricated by physical-vapour deposition (PVD), has a E_g ~ 1.06*e*V, and a $\sigma_{RMS,PVD}$ ~ 65nm, while the CIGSSe is fabricated by rapid-thermal processing (RTP), has a E_g ~ 1.01*e*V, and a $\sigma_{RMS,RTP}$ ~ 120nm. While the current certified, 24.2%-efficient, world-record monolithic CIGSe-perovskite tandem solar cell has previously been achieved with SAM as a stand-alone HTL, this work investigates whether SAM can yield similarly high efficiencies also on industrially compatible, very rough RTP CIGSSe absorbers. We find that the devices with SAM as stand-alone HTL suffer from severe *FF* and V_{oc} losses and that NiO_x:Cu is needed to act as a shunt-quenching layer below that SAM, ensuring conformal coverage of the rough bottom sub-cell surface. Within this work the highest-achieved (in-house measured) *PCE*s for the RTP and PVD CIGS-based tandems are 21.6% and 23.2% respectively, on a cell area of 1.08cm^2, both of which are obtained with NiO_x:Cu + SAM as an HTL.

Keywords

$Cu(In,Ga)(S,Se)_2$; metal-halide perovskite; monolithic tandems; nickel oxide (NiO_x); hole-transporting layers (HTLs).

Abbreviations

1. HTL[1], NiOx(:Cu)[2], SAM[3], PVD[4], RTP[5], MeO-2PACz[6]

1. Introduction

Monolithic copper-indium-gallium-diselenide ($Cu(In,Ga)Se_2$ or shortly,CIGS)/lead-halide-based perovskite tandem solar cells, with their tunable bandgaps [1], cheap processing via various deposition techniques [2]–[4], and their ability to be deposited on flexible substrates [5], [6], present an industrially-attractive approach to overcome the

[1] Hole-transporting layer
[2] Nickel oxide (NiO_x) or copper-doped nickel oxide (NiO_x:Cu)
[3] Self-assembled monolayer
[4] Physical vapor deposition
[5] Rapid thermal processing
[6] [2-(3,6-dimethoxy-9H-carbazol-9-yl)ethyl]phosphonic acid

detailed balance (also known as Shockley-Queisser) limit of efficiency of the single-junction solar cells [7]. Despite the benefits a flexible PV technology offers, current global efforts to develop monolithic tandems largely focus on silicon (Si)/perovskite tandems. This is due to the general promise of higher efficiencies as demonstrated by world record values recently having surpassed the threshold of 30% [8] and the necessity to reach increased growth rates for renewable energy generation. However, CIGS solar cells are characterized by having lower environmental impact than Si [9] and an energy payback time almost twice as fast as that of Si [9]. If fully optimized, a monolithic CIGS-perovskite tandem would have only around 6% lower energy yield compared to a Si-perovskite tandem, under the condition that the Si-perovskite tandem is manufactured on a fully textured Si substrate [10]. Furthermore, monolithic CIGS-perovskite tandems can be manufactured as fully integrated modules on flexible substrates [11], making these tandems attractive for building-integrated PV or space applications where the weight of the solar cells plays a crucial role. With respect to space applications, it has been shown that CIGS-perovskite tandems are proton-radiation hard and retain 85% of their initial efficiency under AM0 solar illumination, even after 68MeV proton irradiation [12]. Si-perovskite tandems, on the other hand, had retained only 1% of their starting PCE under the same conditions [12].

Despite these unique aspects of the monolithic CIGS/perovskite tandem technology, its development has been slowed down by the rough surface of the bottom CIGS sub-cell, which entails the presence of macroscopic defects in the cell stack originating from the fabrication process. Therefore, most of the initial research endeavors in the manufacturing of the CIGS-perovskite tandem solar cells have been directed towards overcoming the issue of this shunt-inducing rough CIGS surface. In 2015, Todorov et al. decreased the surface roughness of the conventional CIGS absorbers by incorporating a solution-processed CIGS and produced the first monolithic CIGS-perovskite tandem solar cell [13]. Similar ideas have been adopted by Uhl et al. [14] and Jang et al. [15] who manufactured tandems with solution-processed and electro-deposited copper indium diselenide ($CuInSe_2$) as the bottom cell. Despite the lower surface roughness, all of these devices were limited in their performance, with Todorov et al. and Uhl et al. reaching 11.0% and Jang et al. reaching 8.55% in *PCE*. The poor performance was ascribed to the organic PEDOT:PSS (poly(3,4-ethylenedioxythiophene):poly(styrenesulfonate)) hole-transporting layer (HTL) that was used in all three devices, primarily because the PEDOT:PSS-perovskite interface has been known to exhibit severe V_{oc} losses [16].

By 2018, Han et al. manufactured a monolithic $Cu(In,Ga)Se_2$-perovskite tandem with a certified *PCE* of 22.43% and a V_{oc} of 1.78V, which remains until now the only tandem device where the V_{oc} in the tandem was equal to the sum of the V_{oc}s of the individual sub-cells [17]. The high performance was obtained by firstly depositing a thick ITO (indium-

doped tin oxide) on top of the rough surface of the bottom-cell stack, then polishing the ITO until a smooth surface was obtained, and finally spin-coating PTAA (poly[bis(4-phenyl)(2,4,6-trimethylphenyl)amine), instead of PEDOT:PSS, as an HTL. This approach of mechanical polishing of the bottom-cell surface is the first testified attempt to decouple the growth of the perovskite top cell from the CIGSe roughness and the first successful demonstration of highly-efficient monolithic CIGSe/perovskite tandem solar cell. However, the 22.43% efficiency was possible only for a 0.042cm^2 cell surface. Already by a cell surface of 0.58cm^2, the efficiency had dropped to 20.8%, showing that the mechanical polishing procedure is not attractive for large-scale and/or industrial applications since it is extremely time- and resources-costly.

By 2019, Jošt et al. obtained a 21.6%-efficient tandem with an area of 0.78cm^2, V_{oc} of 1.58V, *FF* of 76%, and NiO_x-PTAA as HTL bi-layer without any smoothing or treatment of the bottom-cell surface [18]. The atomic-layer deposited (ALD) NiO_x resulted in a closed layer that smoothly covered the rough bottom-cell's surface, while the PTAA passivated the NiO_x-perovskite interface, and further boosted the efficiency of the tandem with NiO_x as a stand-alone HTL which enabled a PCE of 18.0%, a V_{oc} of 1.49V V_{oc}, and a FF of 70.2% FF.

NiO_x and PTAA were omitted as HTLs as soon as organic self-assembled monolayers (SAMs) with phosphonic acid as an anchoring group fully revolutionized the field and were implemented to act as hole-selective layers in metal-halide perovskite solar cells [19]. The strong binding affinity of the SAMs to any oxide surface enables conformal coverage even of rough surfaces and almost lossless SAM-perovskite interface with a minimal QFLS-V_{oc} offset [20]. By incorporating a SAM as an HTL in a monolithic CIGS-perovskite tandem solar cell with an area of slightly more than 1cm^2, Al-Ashouri et al. obtained a certified PCE of 23.3%, V_{oc} of 1.68V, and a *FF* of 71.9% [20]. These results were then soon surpassed by Jošt et al. who currently hold the certified world record at 24.2% *PCE* for the monolithic CIGS-perovskite tandem solar cell with a 71.2% *FF*, 1.77V V_{oc}, 1.05cm^2 cell area using SAM as HTL [21] (blue dot in Figure 1). This tandem solar cell additionally incorporated a thin LiF layer to passivate the perovskite-ETL interface and a PEAI (phenethyl-ammonium iodide) additive in the perovskite solution [21].

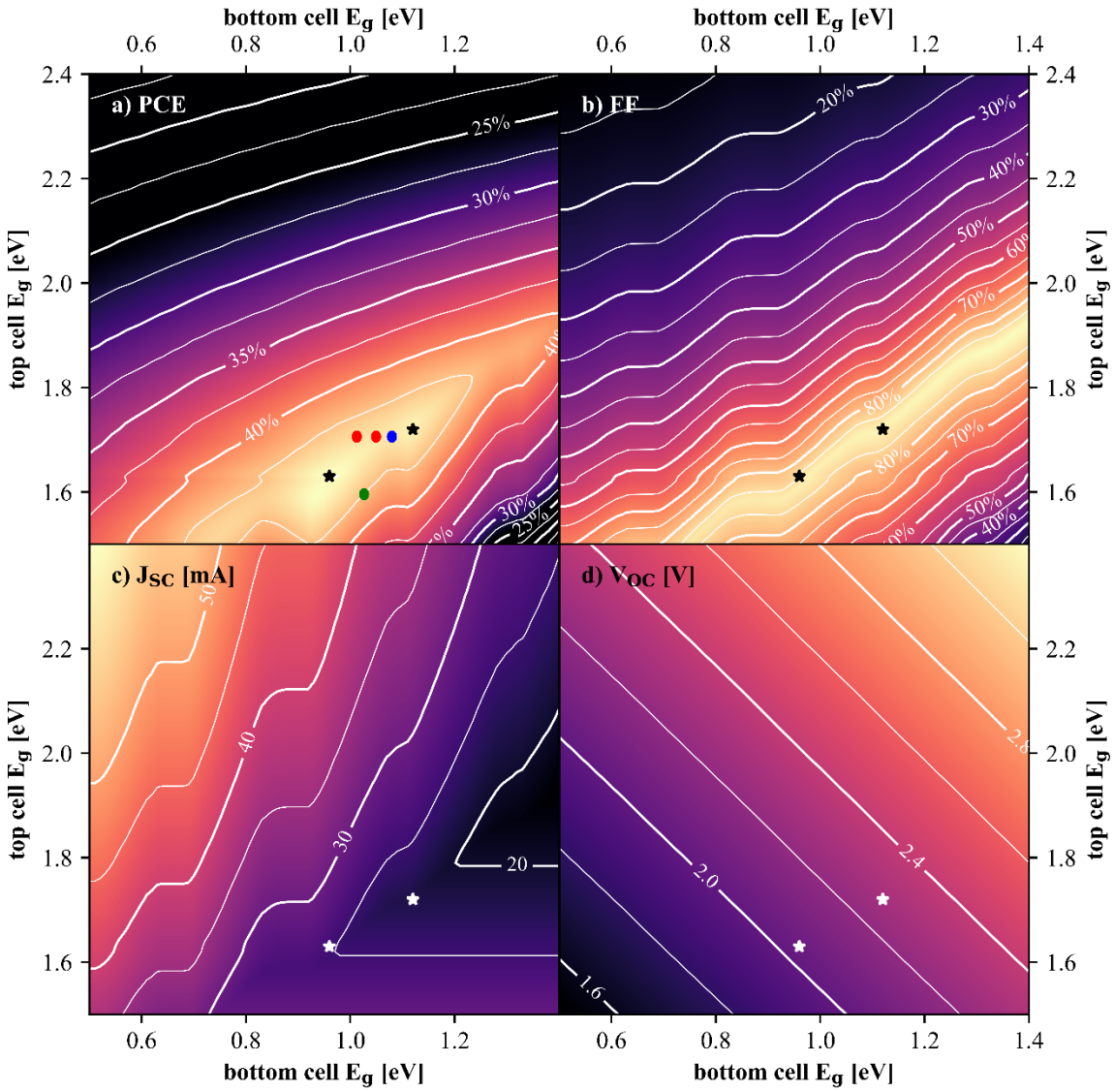

Figure 1: Detailed balance limit of monolithic CIGS-perovskite tandems for varied bottom and top bandgaps. The maximum 45% efficiency (black star) is at a 0.96eV-1.6eV CIGS-perovskite bandgap combination. Secondary maximum is 44.4% (second black star) at a 1.12eV-1.72eV CIGS-perovskite bandgap combination. The world-record device (24.2%) by Jošt et al. [21] is marked with a blue dot; the 23.5% device by Ruiz-Preciado et al. [22] is marked with a green dot; the bandgap combinations used in this work are marked with red dots.

This world-record monolithic CIGS-perovskite tandem solar cell has been achieved with co-evaporated Cu(In,Ga)Se_2

(CIGSe) with a bandgap of ~1.08*e*V and a perovskite bandgap of ~1.67*e*V. However, a detailed balance limit calculation of CIGS-perovskite monolithic tandems with varied bottom (CIGS) and top cell (perovskite) bandgaps (Figure 1) shows that this bandgap combination is slightly off the region for optimum bandgap combination and that combining a CIGS bandgap of ~1.00*e*V with a perovskite bandgap of ~1.65*e*V can yield a theoretical primary maximum efficiency as high as 45% (marked with a black star in Figure 1). Therefore, Ruiz-Preciado et al. have fine-lowered the bandgap of a bottom CIS device down to 1.03eV and by combining it with a 1.59eV top device, they have obtained a certified efficiency of 23.5% on an area of 0.5cm^2 (green dot in Figure 1) [22]. In addition to fine-tuning the bandgaps of the two sub-cells, their Ga-free absorbers displayed a decreased surface roughness compared to the conventional CIGSe or CIGSSe absorbers and by using a NiO_x + 2PACz ([2-(9H-carbazol-9-yl)ethyl]phosphonic acid) as a hole-transporting layer, they obtained a FF as high as 75% [22].

In this work, we decrease the bandgap of the CIGS absorber compared to the work presented by Jošt et al. and compare the performance of CIGS-perovskite monolithic tandems with two differently manufactured CIGS bottom cells. A $Cu(In,Ga)Se_2$ (CIGSe) absorber deposited by co-evaporation (for simplicity, to be referred as physical-vapor deposition (PVD)) [2] has a minimum bandgap of around 1.06*e*V, while the $Cu(In,Ga)(S,Se)_2$ (CIGSSe) absorber deposited by rapid thermal processing (RTP) [3], [4] has a photoactive bandgap of around 1.01*e*V ideal for tandem applications (red dots in Figure 1). Furthermore, the RTP CIGS is industry-compatible due to its fast processing time and its implementation in the 23.35% single-junction CIGS world record device [23].

However, unlike the CIS absorbers with decreased surface roughness presented by Ruiz-Preciado et al. [22], the surface of the RTP cell is almost twice as rough as the surface of the PVD cell ($\sigma_{RMS,RTP}$ ~ 120nm vs. $\sigma_{RMS,PVD}$ ~ 65nm), which, when subjected to a wet-chemical deposition process of the perovskite absorber, may lead to shunts. Additionally, despite the outstanding performance of the current 24.2%-efficient SAM-based champion tandem [21], this device exhibited 5% lower fill factor (*FF*) and worse shunt resistance (R_{sh}) compared to the 21.6%-efficient monolithic CIGS-perovskite tandem with NiO_x + PTAA [18] and 3.8% lower *FF* compared to the 23.5%-efficient monolithic CIS-perovskite tandem with NiOx + 2PACz as an HTL bi-layer [22]. The higher FF of the devices with NiO_x opens up the question whether the SAMs can ensure high performance on the significantly rougher RTP absorbers.

Motivated by this question, this work revisits the idea of incorporating NiO_x as a shunt-quenching layer in an

inorganic-organic HTL bi-layer. To avoid damaging the bottom cell, which is sensitive to temperatures higher than 200°C, the NiO_x was deposited via low-temperature RF (radio frequency) magnetron sputtering. However, low-temperature deposited NiO_x suffers from low crystallinity and a higher amount of surface states, defects, and impurities compared to NiO_x annealed at high temperatures [24]. The most common defect in NiO_x is the Ni^{2+} (Ni in NiO) interstitial vacancy (V_{Ni}^{2+}) [25], which is compensated for by the Ni^{3+} (Ni_2O_3 and NiOOH) species. For low-temperature processing, the number of Ni^{2+} vacancy defects is high since NiOOH species are not eliminated via the usual high-temperature annealing post-deposition treatments. Literature has already pin-pointed that these defects can also cause a loss in conductivity, unfavorable accumulation of holes at the NiO_x-perovskite interface, a high rate of trap-assisted interfacial recombination, reduced collection and extraction of holes, accelerated degradation [26], and even chemical reactions with halogens from the perovskite absorber [27], [28]. Two common approaches to overcome these limitations are to either dope the NiO_x or to chemically treat the NiO_x and passivate its surface defects. Therefore, this work systematically investigates the performance of three HTL configurations - either SAM as stand-alone HTL or NiO_x(:Cu) + SAM bi-layer in monolithic CIGS-perovskite tandem solar cells manufactured either on a PVD CIGSe or an RTP CIGSSe absorbers. Notice that we use NiO_x(:Cu) as a notation to refer simultaneously to both NiO_x and NiO_x:Cu.

2. Methodology

2.1. Manufacturing of the monolithic CIGS-perovskite tandem solar cell

The tandem solar cell stack is shown in Figure 2. The manufacturing of the tandem solar cell is explained starting from the bottom (CIGS) sub-cell, to the HTL (NiO_x(:Cu) + SAM), and to the top (perovskite) sub-cell.

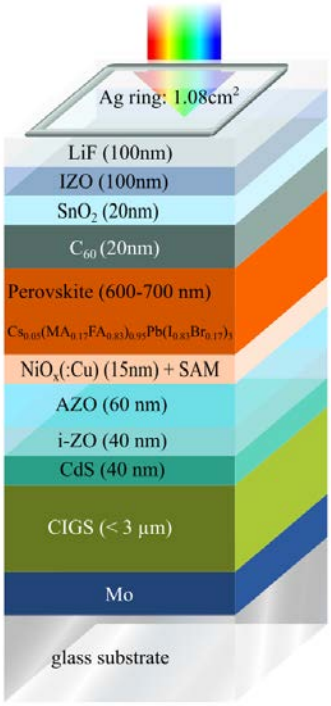

Figure 2: CIGS-perovskite monolithic tandem solar cell stack.

2.1.1. Deposition of the bottom (CIGS) sub-cell

Regardless of whether the CIGS is deposited via co-evaporation or rapid-thermal processing, the substrate for the CIGS absorber is a 1mm thick 5 by 5cm^2 soda-lime glass on top of which a molybdenum (Mo) back contact (~400nm for the RTP CIGS and ~800nm for the co-evaporated CIGS) is deposited via direct-current (DC) magnetron sputtering. Then the PVD CIGSe or RTP CIGSSe absorber is deposited.

The **co-evaporation** of the **Cu(In,Ga)Se$_2$** (CIGSe) absorber is performed in a vacuum-based machine via a three-stage process in which the substrate is placed on a rotating substrate holder above a valved selenium cracker source, and Cu-, In-, Ga-, and RbF-sources [29]. During the first processing step, the substrate is heated to 300°C and Ga_2Se_3 and In_2Se_3 layers are interchangeably deposited. For the second processing step, the substrate temperature is increased to 530°C and Cu-Se is evaporated until the CGI (Cu content/(Ga + In) content) ratio reaches 1 (stoichiometric point). The second processing step is finalized by maintaining a three-minute Cu-rich regime with a CGI of 1.05, improving the film crystallinity [30]–[32]. Finally, in the third processing step, the Cu content is firstly decreased back to stoichiometry, and then to the final Cu-poor $CIGSe_2$ composition with a CGI ratio of ~0.9-0.95. The co-evaporation of the $CIGSe_2$ is finalized with a RbF post-deposition treatment, as explained in [33].

The **rapid thermal processing** of the **$Cu(In,Ga)(S,Se)_2$** (CIGSSe) absorber starts by DC sputtering of copper (Cu), gallium (Ga), and indium (In) from two different targets: CuGa and In. The samples used in this work have a final GGI (Ga content/(Ga + In) content) ratio of ∼0.5, and a final CGI ratio of ∼0.9. To obtain the final $Cu(In,Ga)(S,Se)_2$ absorber, the CuInGa precursor undergoes a two-step chalcogenization (firstly selenization and secondly sulfurization) with rapid-thermal processing (RTP) at atmospheric pressure. The selenium (Se) and the sulfur (S) source are elemental Se vapor and H_2S gas, respectively. The selenization lasts 10 minutes, and is performed at a temperature of 580℃ for the selenization chamber, 440℃ for the crucible, and 800℃ for the cracker. The sulfurization lasts 6 minutes, and is performed at a temperature of 580℃ for the sulfurization chamber, and 400℃ for the cracker. More details on the RTP processing can be found in [4].

After the absorber deposition, the CIGS solar cells are completed with a 40nm CdS (cadmium sulfide), a 40nm i-ZnO (intrinsic zinc oxide), and a 60nm AZO (aluminum-doped zinc oxide) layer. The CdS films are deposited by chemical bath deposition (CBD) into a solution heated to 60℃ and composed of de-ionized (DI) water, Cd-acetate (2.5 mM, purity >98%), thiourea (0.05 M, purity >99%), and aqueous ammonia solution (max. contamination ≤260ppm, the ammonia is GPR RECTAPUR). The CdS layer then grows via the reactions described in [34]. The i-ZO and the AZO form an electron-transporting bi-layer deposited via radio frequency (RF) sputtering. Additionally, the AZO is deposited through a mask to define the active area and prevent current leakage.

2.1.2. Manufacturing of the hole-transporting layer

From ceramic targets (3inch, ∼75mm in diameter, manufacturer Nova Fabrica), 15nm-thick NiO_x (99.9%) or NiO_x:Cu (2% Cu) are deposited through a low-temperature radio-frequency (RF) magnetron sputtering process without intentional heating. The power is kept constant at 60W, target-to-sample distance to ∼5cm, and total pressures $(4.7 \pm 0.2) \times 10^{-3}$mbar for NiO_x and $(4.6 \pm 0.2) \times 10^{-3}$mbar for NiO_x:Cu. The sputtering is performed in pure argon atmosphere (99.999%) at a mass flow-rate of 25 sccm (standard cubic centimeter per minute). To suppress the amount of surface hydroxides, the NiO_x(:Cu) films undergo an air-free transfer from the sputtering chamber to a N_2-filled glovebox where they are sealed and then subjected to a 15-minutes ozone treatment avoiding UV-exposure by means of a filtering sheet of glass. The samples are then moved to a N_2-filled glove box for the deposition of the SAM (either on top of the NiO_x(:Cu) or as a stand-alone HTL).

The SAM used in this work was MeO-2PACz ([2-(3,6-dimethoxy-9H-carbazol-9-yl)ethyl]phosphonic acid) [20].

SAM solution (1mM) is prepared by mixing ~1mg of MeO-2PACz (>98% purity, TCI manufacturer) with 4ml of anhydrous ethanol (VWR chemical) and then subjected to ten-minutes ultrasonic shaking. For the SAM deposition, 100µl of the 1mM solution are slowly dripped in the middle of the sample. There is a three to four seconds waiting time for the solution to spread over the sample. The samples are then spin-coated at 4000 rpm for 45 seconds and then annealed at 100°C for ten minutes. The samples are then transferred through N_2 for the perovskite spin-coating.

2.1.3. Manufacturing of the top (perovskite) sub-cell

The perovskite consistently used throughout this work is the "triple-cation perovskite" (E_g ~ 1.63*e*V): $Cs_{0.05}(MA_{0.17}FA_{0.83})_{0.95}Pb(I_{0.83}Br_{0.17})_3$ [35]. MA and FA are methylammonium (CH_6N^+) and formamidinium ($CH(NH_2)_2$) cations, respectively. Lead iodide (PbI_2, MW = 461.01g/mol, 99.99% purity, TCI manufacturer) and a lead bromide ($PbBr_2$, MW = 367.01g/mol, 99.99% purity, TCI manufacturer) salt with a 4:1 ratio DMF:DMSO mixture (DMF: N,N-Dimethylformamide, MW = 73.09g/mol; DMSO: Dimethylsulfoxid, MW = 78.13g/mol; Sigma-Aldrich manufacturer). The PbI_2 solution is then mixed with a formamidinium iodide salt (FAI, MW = 171.97g/mol , 99.99% purity, dyenamo manufacturer) and the $PbBr_2$ is mixed with a methylammonium bromide salt (MABr, MW = 111.97g/mol, 99.99% purity, dyenamo manufacturer). The cesium iodide salt (CsI, MW = 259.81g/mol, 99.999% Cs) is simply dissolved in DMSO. The final perovskite solution is obtained by mixing $FAPbI_3$ and $MAPbBr_3$ in a 83:17 ratio to constitute 95% of the total perovskite solution and CsI to constitute the last 5% as described in [35]. 100µl of the perovskite solution are dropped in the middle of the sample, and the spin-coating is performed in a rich anti-solvent environment (closed lid) at 4000 rpm for 40 seconds (from which 5s are acceleration time). Ethyl acetate (anhydrous, 99.8% purity, Sigma Aldrich manufacturer) is dropped as an anti-solvent 25 seconds after the start of the spin-coating. The samples are annealed at 100°C for half an hour. Next, 20nm-thick C_{60} (buckminsterfullerene, MW = 720.66g/mol, sublimed, 99.999% purity, CreaPhys GmbH manufacturer) and tin oxide (SnO_2) are deposited via evaporation and atomic layer deposition, respectively. These depositions are elaborated in [36]. Next, a layer of 100nm of indium-zinc-oxide (IZO) layer is sputtered through a mask. A silver (Ag) ring is evaporated through a mask defining the tandem's active area of 1.08cm^2. The tandem solar cells are finalized by evaporating a 100nm anti-reflective lithium-fluoride (LiF) film.

2.2. Characterization

2.2.1. Solar-cell characterization

Each *JV* curve is obtained without previous light-soaking or biasing in either a forward-bias ($V_{start} < V_{end}$) or in a reverse-bias ($V_{start} > V_{end}$) scan direction. The current density-voltage (*JV*) measurements of the tandem devices were performed in air, at a sample temperature of 25°C, with a 12 LED sun simulator (Wavelabs manufacturer, class AAA), under AM1.5G simulated illumination. Two of the contact needles were placed on the tandem's silver ring that defines the cell's area (see Figure 2) and two were contacting the molybdenum (Mo) bottom layer. The calibration of the sun simulator was performed with a RG780 filtered solar cell with a known spectral response. The JV curves were obtained with a Keithley 2600 SMU in a four-point probe measurement configuration and were controlled by a LabView software.

The external quantum efficiency (EQE) measurements were performed with a home-built three-LED (blue, red, green) set-up in a 300nm-770nm and 500nm-1250nm wavelength range for the perovskite and the CIGS cell, respectively. To obtain the EQE spectrum of the CIGS sub-cell, the intensity of the 455nm LED was set in the range from 10 to 45%, the bias voltage was set to 1V, and no bias light was used unless the signal displayed poor noise-to-signal ratio. To obtain the EQE spectrum of the perovskite sub-cell in the tandem, the intensity of the 850nm LED was varied until maximum signal intensity and minimum noise was obtained. The bias voltage was 0.6V and no bias light was used.

2.2.2. Dark lock-in thermography (DLIT), photoluminescence, and confocal microscopy imaging

The dark lock-in thermography (DLIT) images were obtained with a high-resolution Thermosensorik system equipped with a “TDL 640” InSb midwave infrared (MWIR) camera with a focal length of 28mm. Two images are recorded: high- and low-injection at a frequency of 1 Hz and a time of 1 minute.

The photoluminescence (PL) images are obtained by capturing the incoming photons produced during radiative recombination after exiting the material with a light source. An InGaAs camera (measuring from 0.9 to 1.7µm) with an excitation wavelength of 650nm and a software from LumiSolarMobile System from GreatEyes were used for this task. The integration time for the measurement ranges from 15ms to 300ms.

For the confocal-microscopic images, a Keyence microscope (series VK-X) was used. This microscope combines the color information from a combination of a CCD camera and a halogen lamp, and the information from the laser intensity from a laser light photoreceptor facilitating depth perception.

The atomic force microscopy (AFM) pictures/3D maps show the samples surface morphology of a representative 20 by 20 µm area. They were recorded using a XE-70 SPM with a silicon tip (PPP-NCHR) in dynamic mode. The raw data was visualized with the free software Gwyddion.

The scanning electron microscope (SEM) is a Zeiss Merlin FE-SEM. The SEM images were collected at an accelerating voltage of 5keV.

3. Results and discussion

Figure 3 and Table 1 summarize the performance of the six tandem solar cells obtained by using three different HTLs (NiO_x + MeO-2PACz, NiO_x:Cu + MeO-2PACz, and MeO-2PACz as a stand-alone HTL) and two different CIGS absorbers (PVD $Cu(In,Ga)Se_2$ (CIGSe) and RTP $Cu(In,Ga)(S,Se)_2$ (CIGSSe)). Notice that CIGS refers simultaneously to both the PVD CIGSe and RTP CIGSSe absorbers, while referring to them individually will be explicitly written as either CIGSe or CIGSSe.

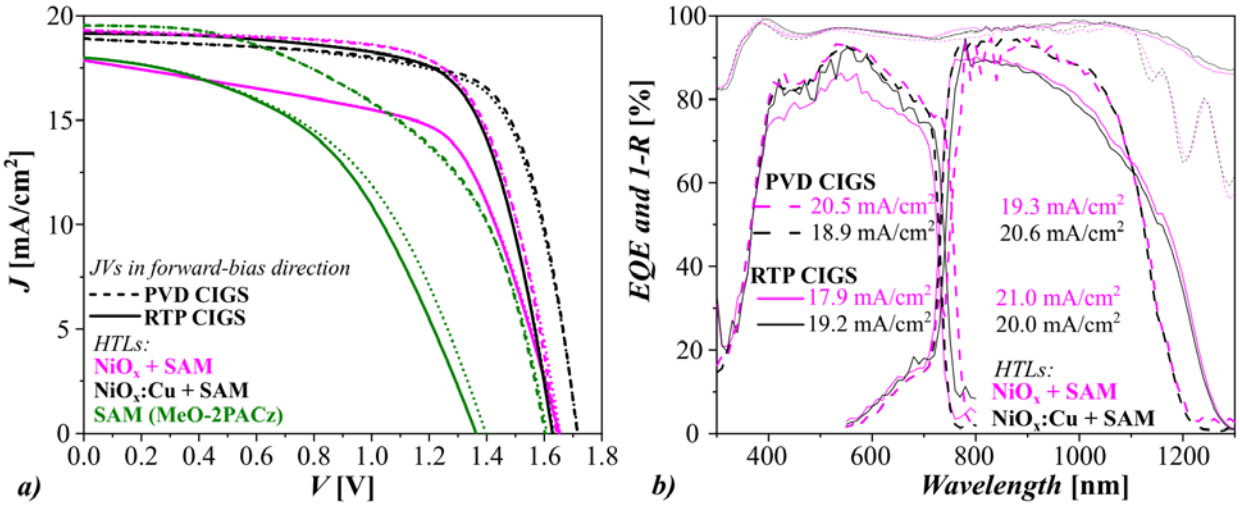

Figure 3: a) *JV* curves measured in forward-bias scan direction (dashed or solid lines) and in reverse-bias scan direction (dotted line) of the devices presented in Table I. Dashed lines are used for the PVD CIGSe absorbers and solid lines are used for the RTP CIGSSe absorbers. The HTLs are denoted with different colors: magenta, black, or green for NiO_x + SAM, NiO_x:Cu + SAM, and SAM as an HTL, respectively. b) EQE, 1-R and EQE-integrated J_{sc} for the NiO_x(:Cu) + SAM devices only.

Cell type	*HTL*	V_{oc} (V)	J_{sc} (mA/cm^2)	*FF* (%)	*PCE* (%)
***PVD* CIGSe**-perovskite monolithic tandem solar cell	NiO_x + SAM	1.66	19.3	69.2	22.2
	NiO_x:Cu + SAM	1.72	18.9	71.3	23.2
	SAM	1.60	19.5	53.1	16.5
***RTP* CIGSSe**-perovskite monolithic tandem solar cell	NiO_x + SAM	1.65	17.9	60.6	17.9
	NiO_x:Cu + SAM	1.63	19.2	69.1	21.6
	SAM	1.36	18.0	47.3	11.6

Table 1: Solar-cell parameters for CIGS-perovskite monolithic tandem solar cells in forward direction with two different types of CIGS (PVD CIGSe vs. RTP CIGSSe) and three different hole-transporting layers - NiO_x + SAM, NiO_x:Cu + SAM and SAM - where SAM is always the MeO-2PACz self-assembled monolayer.

NiO_x:Cu + SAM is the most-efficient HTL for both PVD and RTP-based CIGS tandem devices. The champion PVD CIGSe-based tandem solar cell has an (in-house measured) *PCE* of 23.2%, *FF* of 71.3%, and a V_{oc} of 1.72V. The champion RTP CIGSSe-based tandem solar cell has a promising *PCE* of 21.6% and its 1.6% loss in the *PCE* compared to the PVD CIGSe -based tandems is mostly due to 90mV V_{oc} losses.

NiO_x + SAM is the second-best HTL, with a *PCE* of 22.2% and 17.9% in the PVD and RTP CIGS-based tandems, respectively. Unlike the tandems with NiO_x:Cu + SAM, the tandems with NiO_x + SAM do not experience V_{oc} losses as the CIGS is changed from PVD to RTP ($V_{oc,PVD-CIGSe}$ = 1.66V vs. $V_{oc,RTP-CIGSSe}$ = 1.65V). Instead, the major PCE loss for the RTP compared to the PVD CIGS-based tandem devices with NiO_x + SAM is caused by a prominent ~9% loss in *FF*.

With respect to the short-circuit current density, the EQE measurements of the NiO_x(:Cu) + SAM devices indicate that - with the exception of the RTP CIGSSe with NiO_x + SAM - the devices are relatively well current-matched. However, although the lower bandgap for the RTP CIGSSe has been successfully achieved, the RTP CIGSSe-based tandem devices do not display significantly higher J_{sc} values than the PVD CIGSe-based tandem devices due to a lower red-light response of RTP samples. This low red-light response can be due to insufficient diffusion length and/or insufficient thickness. The overall thickness of the RTP CIGS absorber would be sufficient for good absorption if about half of the thickness in the back of the absorber was not consisting of a wide-bandgap material with a high Ga content that hardly contributes to the long-wavelength absorption. Since the overall GGI of the RTP CIGS is 0.5, the films are effectively half CIS (on top) and half CGS (at the bottom), yielding optical losses in the long-wavelength regime.

Finally, the devices with SAM as a stand-alone HTL suffer from a low *FF* in both the RTP and the PVD CIGS- based tandems and additionally from a low V_{oc} (1.36V) in the RTP CIGSSe-based devices. The *FF* in both devices is also poor, indicating severe shunting behavior. The poor *FF* and R_{sh} also prevented the EQE measurements (Figure 3b) to be performed for the SAM-based tandem solar cells.

Next, we move on to investigating the shunting behavior of the tandem devices. Before discussing the impact of the different CIGS absorber on the tandems' performance and shunting, we perform a scanning electron microscopy (SEM) and atomic force microscopy (AFM) imaging on the different CIGSe and CIGSSe absorbers. These images confirm that there is a significant difference in the surface roughness of the PVD CIGSe and the RTP CIGSSe absorbers, confirming that monolithic CIGSSe-perovskite tandems are possible, if the HTL is appropriately chosen.

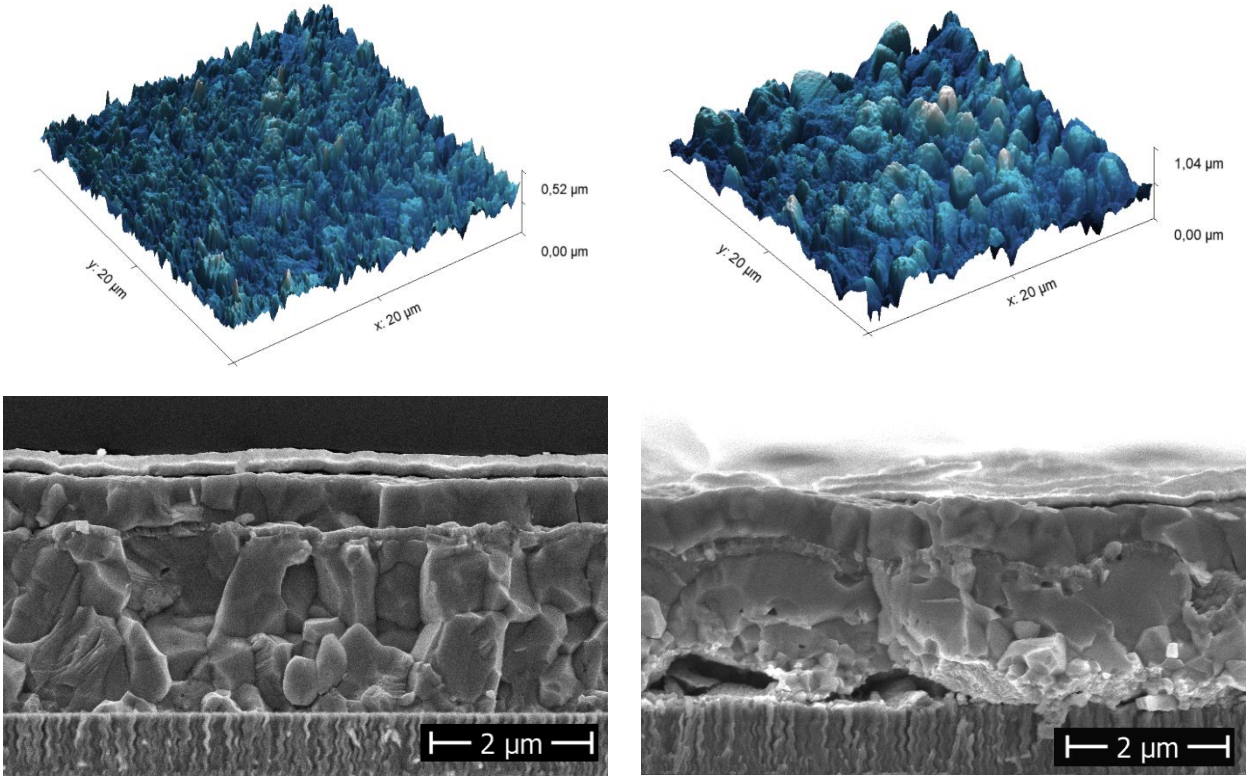

Figure 4: AFM (upper row) and SEM (lower row) images of RTP CIGSe (left-hand side) and of RTP CIGSSe (right-hand side). Both reveal a significantly higher surface roughness of the RTP CIGSSe absorbers. SEM imaging reveals $\sigma_{RMS,PVD}$ ~ 65nm and $\sigma_{RMS,RTP}$ ~ 120nm.

To further investigate the shunting behavior of the tandem devices, photoluminescence (PL), dark lock-in thermography (DLIT), and confocal microscopy images were taken. The PL measurements were performed on the bottom CIGS cells prior to their integration in the tandem devices, while the DLIT and confocal microscopy images

were performed on the finished tandems. In this way, we are looking for possible correlation in the PL-detected defects in the bottom cell and the DLIT/microscopy-detected shunts in the finished tandem solar cells. This approach enables a systematic investigation of the origin of the shunting in the tandem devices: either in the bottom device (be it due to its rough surface, vacancies, or macroscopic defects, which are often non-avoidable for the CIGS devices), or in the variation in the HTL configuration, that then influences the growth of the top cell.

The DLIT measurements of the solar cells are performed by applying a pulsed voltage in the dark [37]. If the dark current that flows through the cell encounters a shunt, the current increases locally, resulting in heat dissipation, and yielding hot spots which are then displayed in the DLIT image [37]. Understanding the nature of these hot spots and their behavior under different biasing condition also enables a distinction between linear (Ohmic) and nonlinear shunts to be made. This is achieved by collecting DLIT images both at high and low injection and in forward and reverse bias **[37]**. Since the Ohmic shunts appear when a current flows through a conductor with a significant Ohmic resistance and radiates heat (also known as Joule heat) **[38]**, the hot spot caused by an Ohmic shunt is detected in both, low and high- injection of the DLIT measurements. If the hot spot disappears in the low-injection, reverse-bias mode, then the shunt is non-linear **[37]**. Out of these two types of shunts, the Ohmic shunts are more severely limiting the devices, resulting in non-negligible V_{oc}, *FF* and R_{sh} losses.

Starting with the **RTP CIGSSe**-based tandem devices, we detect one prominent and one small non-linear shunt for the devices with NiO_x + SAM (*PCE* = 17.9%, Figure 5a) or NiO_x:Cu + SAM (*PCE* = 21.6%, Figure 5b) as an HTL, but no Ohmic shunts. The PL images of the bottom CIGSSe cell implemented in the tandem with NiO_x + SAM (Figure 5a) as an HTL bi-layer displays several dark point defects, out of which two are on the same location as the non-linear shunts detected in the DLIT images, implying that these non-linear shunts in the finished tandem very likely originate from the bottom device. The bottom device implemented in the tandems with NiO_x:Cu + SAM (Figure 5b) shows no such point defects in the bottom device, meaning that the DLIT-detected non-linear shunts have very likely formed during the manufacturing of the top cell.

We also point out that we detect a gradient in the PL images in Figure 5, but not in Figure 7. It is likely that this gradient comes from an edge effect, which we have seen multiple times in our RTP CIGSSe, but not in our PVD CIGSe devices, indicating that our excitation distribution and measurement are correct. The PL gradient could also point to a V_{oc} gradient along the absorber's area. However, as the V_{oc} is proportional to the logarithm of the PL intensity

($V_{oc} \propto \log(PL_{intensity})$), the expected V_{oc} variations should not be too prominent. Nevertheless, this gradient is problematic and future investigation is required to solve this issue and further improve the efficiency of our RTP CIGSSe devices.

The confocal-microscopy images of the CIGSSe-based tandem devices with NiO_x + SAM (Figure 6a) and NiO_x:Cu + SAM (Figure 6b) display similarly-looking brighter spots. A zoomed-in view reveals that these are not pin holes, correlating well to the absence of Ohmic shunts in the DLIT measurements. However, the spot density is more severe for the sample with NiO_x + SAM as an HTL configuration (Figure 6a), which additionally also suffers from minor smudges. These spots could potentially be a result of worsened crystallization of the perovskite absorber, for instance due to the rough RTP surface, due to the HTL, or even due to the anti-solvent-induced wrinkling of the perovskite **[39]**. The combined effect of these microscopy-detected spots in the finished tandem and the PL-detected point-defects in the bottom device could explain why the tandem with NiO_x + SAM as an HTL bi-layer displays a 9% loss in FF compared to the tandem with NiO_x:Cu + SAM (see Table 1).

Finally, the DLIT measurements of the champion device with SAM as a stand-alone HTL with an RTP CIGSSe as the bottom device (*PCE* = 12%, Figure 5c) indicate many severe non-linear shunts in high and low, forward injection mode and several Ohmic shunts and non-homogeneous heat dissipation at low, reverse injection mode. The PL signal (Figure 5c) displays one dominant bright spot at a similar location as one of the non-linear shunts, but no correlation to the Ohmic shunts. This implies that the bottom cell here likely induces one of the non-linear shunts, but that the remaining shunts have appeared during the HTL and the top cell manufacturing. A closer look at the location of the two Ohmic shunts with the confocal microscope (orange and green rectangular areas marked in Figure 5c and Figure 6c) reveals multiple pin-hole structures. Due to the lack of defects in the bottom sub-cell and since the HTL is the only changed parameter among these three devices manufactured on RTP CIGSSe, these Ohmic shunts could be caused by the SAM's inability to cover the much rougher RTP CIGSSe surface (vs. PVD CIGSe), eventually yielding a direct contact between the AZO and the perovskite absorber. However, other reasons could also be mechanical damage in the top or bottom cell during the manufacturing of the tandem devices, both of which are not straightforward to be detected after the tandem has been completed.

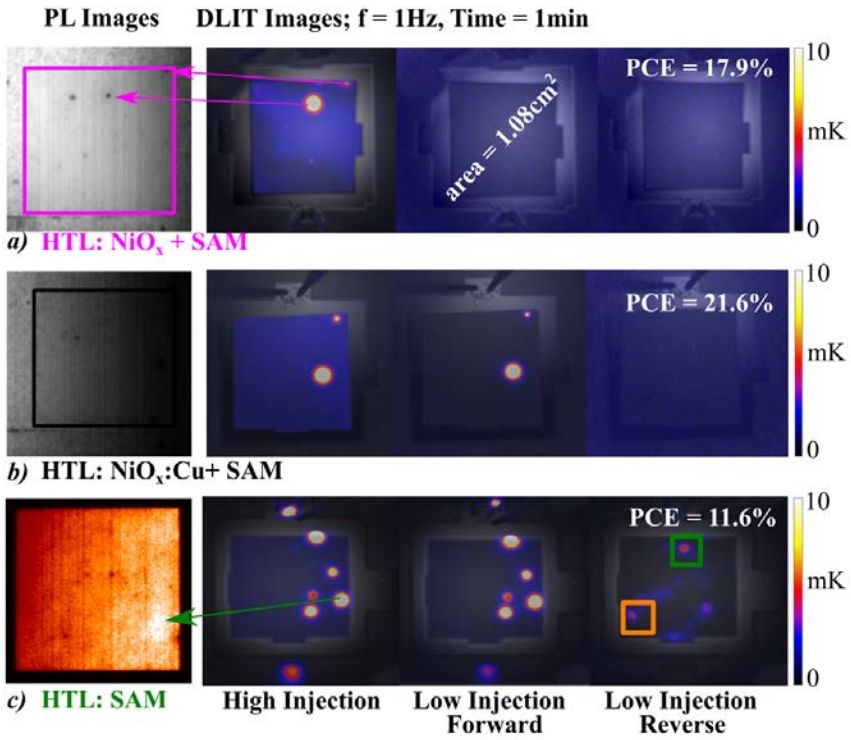

Figure 5: PL (left side) of the RTP CIGSSe absorbers and the DLIT images of the finished tandem solar cells with these absorbers and a) NiO_x + SAM, b) NiO_x:Cu + SAM, and c) SAM as an HTL configuration. The active area of 1.08cm^2 is marked by the colored square in the PL images performed on the CIGSSe absorber and by the top contact silver ring on the finished tandem devices in the complete tandem solar cells.

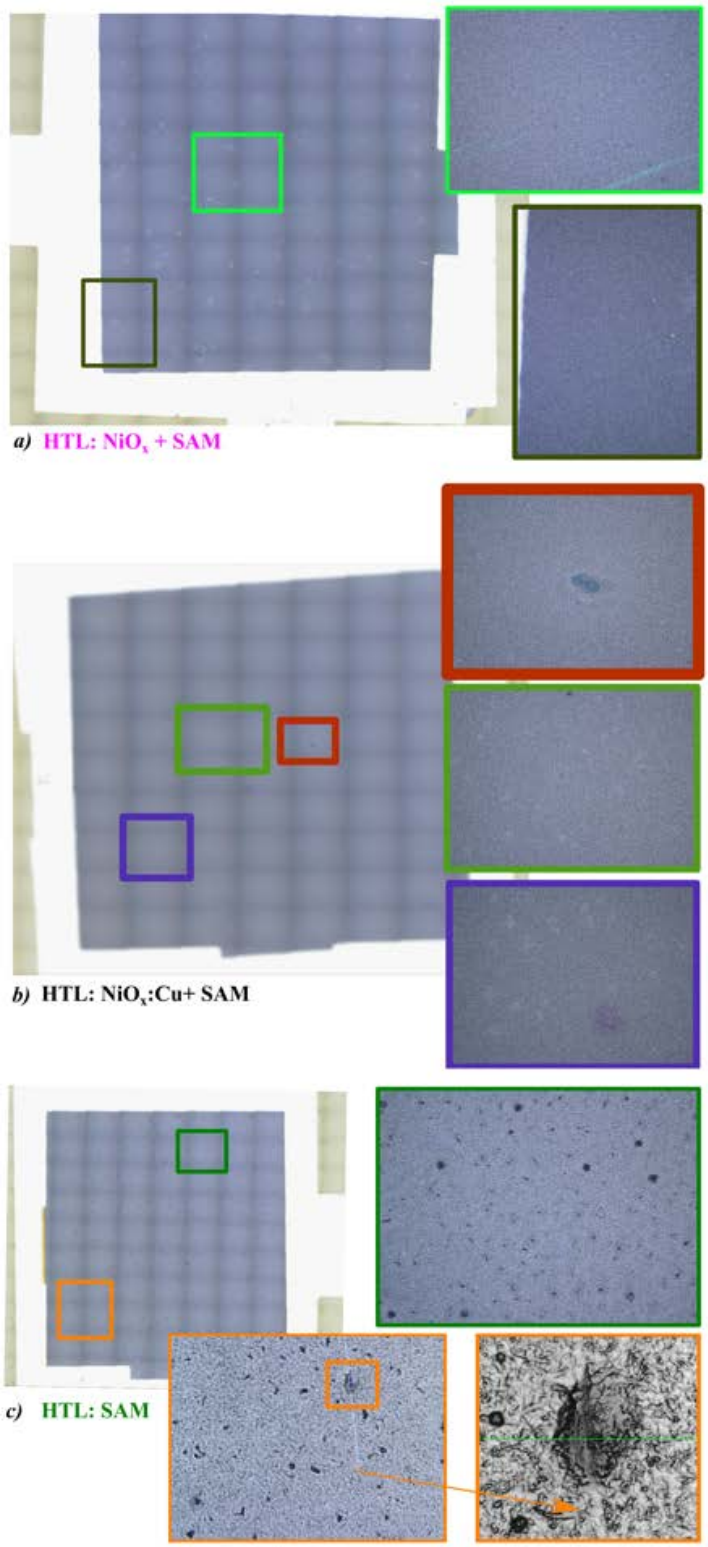

Figure 6: Confocal microscope images of the RTP CIGSSe-based tandem solar cells with a) NiO_x+SAM, b) NiO_x:Cu + SAM, and c) SAM as an HTL configuration

Next, PL, DLIT and confocal microscope images are performed on the tandems with **PVD CIGSe**-based as the bottom sub-cell. All three PL bottom-cell images (Figure 7 a-c, left-hand side) indicate a comparable quality of the PVD CIGSe cells as they all display several dark spots on the right side of the active area.

For the samples with NiO_x + SAM (*PCE* = 22.2%, Figure 7a), the DLIT images indicate non-homogenous heat dissipation at two of the edges of the silver ring and one Ohmic shunt originating at/around the silver ring as well. This Ohmic shunt is caused neither by the bottom nor by the top sub-cell manufacturing. Instead, the confocal microscopy images (Figure 8a) reveal a needle-punctured silver ring. The puncturing occurred during the 4-point *JV* measurements, which were performed before the DLIT/confocal microscopy images. Therefore, the Ohmic shunt was formed after the tandem solar cell with PVD CIGSe and NiO_x + SAM as an HTL bi-layer was characterized, explaining why its *PCE* is as high as 22.2%.

For the samples with NiO_x:Cu + SAM (*PCE* = 23.2%, Figure 7b), we detect inhomogeneous heat dissipation at the silver ring and one non-linear shunt, uncorrelated to the dark PL-detected spots. Similar to the RTP CIGSSe-based tandem devices, this non-linear shunt is very likely formed during the deposition of the top sub-cell in the tandem. However, in the absence of Ohmic and other non-linear shunts, as well as a macroscopic defect-free active area as indicated by the confocal microscope images (Figure 8b), this device is unsurprisingly yielding a high V_{oc} of 1.72V, *FF* of 71.3%, and a *PCE* of 23.2%.

For the samples with SAM (*PCE* = 16.6%, Figure 7c), the PL images display no particular differences compared to the PL images of the CIGSe that was used in the tandems with NiO_x(:Cu) + SAM. Additionally, the DLIT images show that the tandem had homogenous heat dissipation and no Ohmic shunts, but it did have four non-linear shunts at different location than the PL-detected dark spots on the CIGSe cells. The topography investigated via the confocal-microscopy measurements (Figure 8c) displays defects around the Ag ring, protruding the active area and pin-holes-like structures similar to the pinholes detected on the RTP CIGSSe-based tandems with SAM as the stand-alone HTL. Since this SAM-based tandem was manufactured on a CIGSe absorber from the same deposition run as the CIGSe used for the champion device and since the DLIT measurements indicate no Ohmic shunts, one can ascribe the loss in the efficiency and the film structure solely to the HTL.

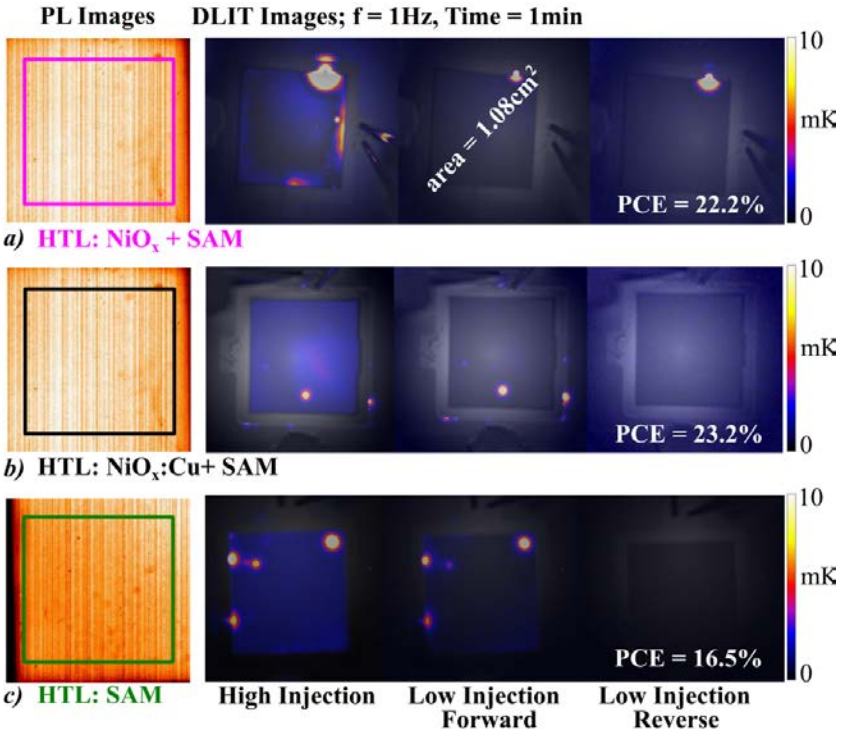

Figure 7: PL (left side) of the PVD CIGSe absorbers and the DLIT images of the finished tandem solar cells with these absorbers and a) NiO_x + SAM, b) NiO_x:Cu + SAM, and c) SAM as an HTL configuration. The active area of 1.08cm^2 is marked by the colored square in the PL images performed on the CIGSe absorber and by the silver ring on the finished tandem devices in the complete tandem solar cells.

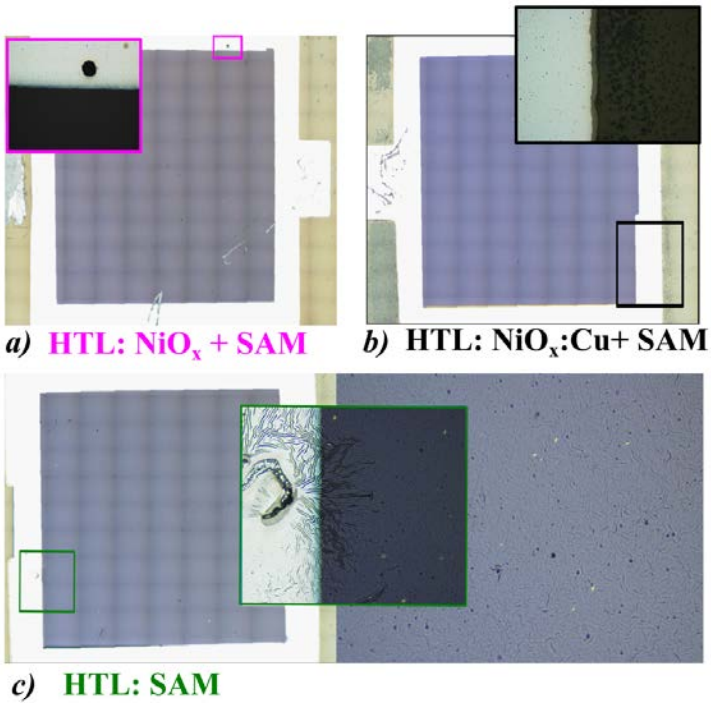

Figure 8: Confocal microscope images of the PVD CIGSe-based tandem solar cells with a) NiO_x+SAM, b) NiO_x:Cu + SAM, and c) SAM as an HTL configuration

Cross-comparing the PL/DLIT images and the performance of each HTL in the RTP or the PVD-based CIGS, one can see that the shunts influence the *FF* most prominently, which then becomes the determining factor for the high performance of the tandem solar cells. On the one hand, NiO_x + SAM can yield high V_{oc} in both the RTP and the PVD-based CIGS tandems (1.66-1.67V for the PVD CIGSe and 1.65-1.66V for the RTP CIGSSe). However, the non-linear shunts originating from the bottom device and the macroscopic defects originating from the top device, yield a ~9% loss in the *FF*, severely limiting the overall tandem performance.

On the other hand, while NiO_x:Cu + SAM displays ~90mV loss in the V_{oc} as the bottom sub-cell is changed from PVD CIGSe to RTP CIGSSe, the *FF* changes by less than 2% because there is no correlation between the non-linear shunts in the tandem and the PL-detected defects in the bottom device. However, it is important to remark that the ~90mV V_{oc} loss in the RTP CIGSSe-based tandems with NiO_x:Cu + SAM as HTL is mostly caused by the bottom sub-cell and not by the NiO_x:Cu + SAM hole-transporting bi-layer. Namely, since the PVD CIGSe cells undergo RbF post-deposition treatment and the RTP CIGSSe cells do not, the PVD CIGSe cells are characterized with a higher V_{oc} compared to the RTP CIGSSe cells. Since the tandem's V_{oc} is the sum of the V_{oc}-s of the individual sub-cells ($V_{oc,tandem}$

= $V_{oc,CIGS}$ + $V_{oc,perovskite}$), the V_{oc} of the RTP CIGSSe cells limits the maximum V_{oc} in the tandem. Therefore, although NiO_x:Cu + SAM can enable higher V_{oc} in the top sub-cell compared to NiO_x + SAM – as seen in the PVD CIGSe-based tandem solar cells – reaching a V_{oc} ~ 1.7V in the RTP CIGSSe-based tandem solar cells is not straightforward. However, if fully optimized, the gain in the J_{sc} in the RTP CIGSSe-based tandem solar cells due to their lower bandgap compared to the PVD CIGSe could potentially compensate for these V_{oc} losses.

The *FF* is also the most affected parameter when SAM is used as an HTL. In the tandem solar cells with PVD CIGSe absorbers, which have also been used in the current world-record 24.2%-efficient monolithic CIGSe-perovskite tandem solar cell, the V_{oc} of the devices with NiO_x + SAM and SAM as a stand-alone HTL differs only by 50-60mV. However, the *FF* of the devices with SAM is lower by 16% and 18% compared to the devices with NiO_x + SAM and NiO_x:Cu + SAM, respectively. In the RTP CIGSSe-based tandem solar cells, SAM also yields non-negligible V_{oc} losses of ~200-300mV, probably caused by the DLIT-detected Ohmic shunts.

Finally, we take a brief look whether incorporating a different absorber in the bottom sub-cell influences the maximum power point (MPP) of the tandem devices. As an initial attempt, we perform five-minutes MPP tracking of three tandems: two with RTP CIGSSe and one with PVD CIGSe as bottom-cell absorbers (Figure 9). The devices with SAM as an HTL were omitted due to their poor performance, while the tandem with PVD CIGSe and NiO_x:Cu + SAM was damaged during the JV and EQE measurements and thus, its MPP tracking was not possible.

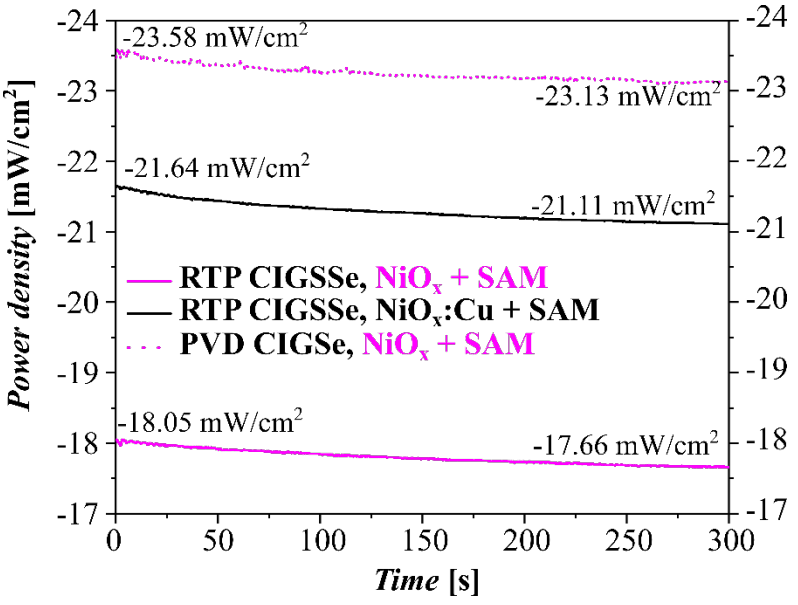

Figure 9: Five-minutes MPP tracking of the monolithic CIG(S)Se – perovskite tandem solar cells with RTP CIGSSe

(solid lines) and PVD CIGSe (dashed line) as a bottom-cell absorber and NiO_x or NiO_x:Cu + SAM as an HTL. All of the devices retain around 98% of their initial MPP.

We do not notice any obvious differences in the short-term stability of the prototype devices and they all retain around 98% of their initial MPP after 5 minutes MPP tracking. However, this measurement cannot be considered a true stability tracking of our tandems since there are many parameters that could influence the tandems' stability and therefore, they should be investigated one by one. For instance, on the bottom-cell side, it could very well be that the roughness and other properties (e.g., the content and mobility of sodium ions) of the RTP absorber also affect the stability. A well-known example is the reduced damp-heat stability of transparent conductive oxides on rough substrates **[40]**. On the top-cell side, it has been shown that a hysteresis in the JV measurements can be an indication of ion migration in the perovskite, affecting also the stability of the devices **[41]–[43]**. As we do not detect a prominent hysteresis in neither the RTP CIGSSe nor the PVD CIGSe devices with NiO_x(:Cu) + SAM devices, but we do detect a hysteresis in the RTP CIGSSe devices with SAM as a stand-alone HTL (see Figure 3), one can hypothesize that SAM induces also an ion migration into the RTP CIGSSe-based tandem devices. However, the stability of the devices containing perovskites is a broad subject, and requires a separate study that would incorporate damp-heat, light- or bias-soaking as well as outdoor measurements that all go beyond the scope of this paper.

Nevertheless, we successfully show that the NiO_x:Cu + SAM hole-transporting bi-layer is the only HTL configuration in this work that decouples the growth of the top perovskite sub-cell from the very rough surface of the RTP CIGSSe absorber and its high macroscopic defect density. Hence, adopting NiO_x:Cu as a shunt-quenching layer below the SAM is a simple approach to eliminate the need for complex polishing of the bottom cell surface introduced by Han et al. [17], for altering the industry-compatible deposition procedure of the RTP CIGSSe absorber as explored by Todorov et al. [13], or for changing to a CIS absorbers as explored by Ruiz-Preciado et al. **[22]**. Additionally, compared to the work by Jošt et al. **[18]** and Ruiz-Preciado et al. **[22]** who used undoped NiOx, we have succeeded in boosting the V_{oc} of the tandems with NiO_x + SAM by using the NiO_x:Cu + SAM HTL bi-layer. The effect of the Cu doping on the NiO_x in previous research has shown that the NiO_x:Cu leads to favorable shift in the valence-band maximum (VBM), increases the NiO_x's conductivity and decreases the Shockley-Read-Hall (SRH) recombination losses **[44]**. Furthermore, NiO_x:Cu has been shown to yield smooth, pin-hole-free HTLs with a large uniformity over large areas, enabling highly-efficient and stable perovskite single-junction devices deposited on both rigid and flexible substrates **[45]**.

Therefore, since NiO_x:Cu ensures conformal coverage of the rough CIGSSe surface and boosts the V_{oc} that is obtained with NiO_x only on the one hand, and since SAM passivates the surface defects of the low-temperature sputtered NiO_x:Cu and boosts the tandem efficiency on the other hand, this work successfully demonstrates the first highly-efficient monolithic CIGSSe-perovskite tandem solar cell with a cell areas above $1cm^2$.

4. Conclusion

In this work we have shown a proof-of-concept that NiO_x:Cu can act as a promising shunt-quenching layer below SAM in both PVD and RTP CIGS-based tandem solar cells. Introducing low-temperature sputtered, 2% Cu-doped NiO_x as a novel inorganic shunt-quenching layer in the monolithic CIGS-perovskite tandem solar cell has enabled us to manufacture the first ever highly-efficient (in-house measured PCE = 21.6%) monolithic tandem solar cell with an active area of $1.08cm^2$ on considerably rough RTP CIGSSe absorbers. Compared to NiO_x + SAM, which yields non-negligible *FF* losses, NiO_x:Cu + SAM succeeds in disentangling the growth of the top device from the non-avoidable structural/morphological or other device defects in the bottom device. This achievement is of paramount importance for the further development and possible up-scaling and industrialization of the monolithic CIGS-perovskite tandem solar cells, since using SAM as a stand-alone HTL on the industrially-compatible RTP CIGSSe absorbers has resulted in pin-hole rich perovskite absorber and therefore, shunted tandem devices.

The here-presented results show that the rough surface is not limiting the tandem's performance when the NiO_x:Cu + SAM HTL bi-layer configuration is used. The achievement is ascribed to combining the best characteristics of both HTLs: on the one hand, the NiO_x:Cu's ability to conformally cover the rough bottom sub-cell surface and prevent the shunt-inducing contact between the AZO and the perovskite, and on the other hand, the SAM's ability to passivate the NiO_x:Cu surface and enable the high efficiency.

Showing that monolithic tandems on very rough absorbers can, in principle, be prepared without a loss in fill factor is only the first step, a proof of concept. It is surely conceivable that the roughness influences the statistical distribution of cell performance parameters. However, this is beyond the scope of the presented initial work where a statistical evaluation would be inappropriate due to the limited number of devices prepared and studied. The statistical evaluation would need to be a subject of a follow-up study.

Therefore, future endeavors should focus on testing the reproducibility and yield of the tandems device's fabrication processes as well as improving the spectral response of the RTP CIGSSe devices in the long wavelength region. On

the side of the HTL, one can investigate the usage of self-assembled monolayers different from MeO-2PACz, variation in the Cu doping in the NiO_x films, or introducing novel dopants altogether. Furthermore, LiF can be deposited as a passivation layer at the ETL-perovskite interface, and additives in the perovskite solution that would improve its crystallization should also be explored in the future, similarly to the current world-record device [21].

ACKNOWLEDGMENTS

The authors would like to thank B. Bunn, J. Lauche, T. Münchenberg, E. Waack, R. Haberecht, A. Steigert, K. Mayer-Stillrich, M. Hartig, M. Kirsch and N. El-Ganainy for technical support during device fabrication. In addition, T. Hänel, K. Mack, J. N. Kleesiek and S. Janke are thankfully acknowledged for support in device characterization. We also acknowledge R. Klenk for the in-depth discussion and proof-reading of the manuscript.

The authors would also like to acknowledge the funding by the Bundesministerium für Wirtschaft und Energie for the speedCIGS project (#0324095D)

REFERENCES

[1] N. J. Jeon *et al.*, "Compositional engineering of perovskite materials for high-performance solar cells," *Nature*, vol. 517, no. 7535, pp. 476–480, Jan. 2015, doi: 10.1038/nature14133.

[2] M. D. Heinemann *et al.*, "Evolution of opto-electronic properties during film formation of complex semiconductors," *Sci. Rep.*, vol. 7, no. 1, p. 45463, Apr. 2017, doi: 10.1038/srep45463.

[3] M. Langhorst *et al.*, "Control of CIGS roughness by initial selenization temperature," in *2015 IEEE 42nd Photovoltaic Specialist Conference (PVSC)*, Jun. 2015, pp. 1–4. doi: 10.1109/PVSC.2015.7356222.

[4] F. Basulto and G. Antonio, "CIGSSe thin film photovoltaic yield improvement for operating conditions," 2021, doi: 10.14279/depositonce-12576.

[5] R. Caballero, C. A. Kaufmann, T. Eisenbarth, T. Unold, R. Klenk, and H.-W. Schock, "High efficiency low temperature grown Cu(In,Ga)Se2 thin film solar cells on flexible substrates using NaF precursor layers," *Prog. Photovolt. Res. Appl.*, vol. 19, no. 5, pp. 547–551, 2011, doi: 10.1002/pip.1064.

[6] H. Zhang *et al.*, "Pinhole-Free and Surface-Nanostructured NiOx Film by Room-Temperature Solution Process for High-Performance Flexible Perovskite Solar Cells with Good Stability and Reproducibility," *ACS Nano*, vol. 10, no. 1, pp. 1503–1511, Jan. 2016, doi: 10.1021/acsnano.5b07043.

[7] W. Shockley and H. J. Queisser, "Detailed Balance Limit of Efficiency of p-n Junction Solar Cells," *J. Appl. Phys.*, vol. 32, no. 3, pp. 510–519, Mar. 1961, doi: 10.1063/1.1736034.

[8] "Best Research-Cell Efficiency Chart." https://www.nrel.gov/pv/cell-efficiency.html (accessed Dec. 20, 2021).

[9] I. Celik *et al.*, "Environmental analysis of perovskites and other relevant solar cell technologies in a tandem configuration," *Energy Environ. Sci.*, vol. 10, no. 9, pp. 1874–1884, Sep. 2017, doi: 10.1039/C7EE01650F.

[10] M. Jošt *et al.*, "Perovskite/CIGS tandem solar cells - can they catch up with perovskite/c-Si tandems?," in *2020 47th IEEE Photovoltaic Specialists Conference (PVSC)*, Jun. 2020, pp. 0763–0766. doi: 10.1109/PVSC45281.2020.9300726.

[11] F. Fu *et al.*, "Flexible perovskite/Cu(In,Ga)Se2 monolithic tandem solar cells," *ArXiv190710330 Cond-Mat Physicsphysics*, Jul. 2019, Accessed: May 07, 2022. [Online]. Available: http://arxiv.org/abs/1907.10330

[12] F. Lang *et al.*, "Proton Radiation Hardness of Perovskite Tandem Photovoltaics," *Joule*, vol. 4, no. 5, pp. 1054–1069, May 2020, doi: 10.1016/j.joule.2020.03.006.

[13] T. Todorov *et al.*, "Monolithic Perovskite-CIGS Tandem Solar Cells via In Situ Band Gap Engineering," *Adv. Energy Mater.*, vol. 5, no. 23, p. 1500799, Dec. 2015, doi: 10.1002/aenm.201500799.

[14] A. R. Uhl *et al.*, "Solution-Processed Low-Bandgap CuIn(S,Se)2 Absorbers for High-Efficiency Single-Junction and Monolithic Chalcopyrite-Perovskite Tandem Solar Cells," *Adv. Energy Mater.*, vol. 8, no. 27, p. 1801254, 2018, doi: 10.1002/aenm.201801254.

[15] Y. H. Jang, J. M. Lee, J. W. Seo, I. Kim, and D.-K. Lee, "Monolithic tandem solar cells comprising electrodeposited CuInSe2 and perovskite solar cells with a nanoparticulate ZnO buffer layer," *J. Mater. Chem. A*, vol. 5, no. 36, pp. 19439–19446, Sep. 2017, doi: 10.1039/C7TA06163C.

[16] L. Meng, J. You, T.-F. Guo, and Y. Yang, "Recent Advances in the Inverted Planar Structure of Perovskite Solar Cells," *Acc. Chem. Res.*, vol. 49, no. 1, pp. 155–165, Jan. 2016, doi: 10.1021/acs.accounts.5b00404.

[17] Q. Han *et al.*, "High-performance perovskite/Cu(In,Ga)Se $_2$ monolithic tandem solar cells," *Science*, vol. 361, no. 6405, pp. 904–908, Aug. 2018, doi: 10.1126/science.aat5055.

[18] M. Jošt *et al.*, "21.6%-Efficient Monolithic Perovskite/Cu(In,Ga)Se2 Tandem Solar Cells with Thin Conformal Hole Transport Layers for Integration on Rough Bottom Cell Surfaces," *ACS Energy Lett.*, vol. 4, no. 2, pp. 583–590, Feb. 2019, doi: 10.1021/acsenergylett.9b00135.

[19] A. Magomedov *et al.*, "Self-Assembled Hole Transporting Monolayer for Highly Efficient Perovskite Solar Cells," *Adv. Energy Mater.*, vol. 8, no. 32, p. 1801892, 2018, doi: 10.1002/aenm.201801892.

[20] A. Al-Ashouri *et al.*, "Conformal monolayer contacts with lossless interfaces for perovskite single junction and monolithic tandem solar cells," *Energy Environ. Sci.*, vol. 12, no. 11, pp. 3356–3369, 2019, doi: 10.1039/C9EE02268F.

[21] M. Jošt *et al.*, "Perovskite/CIGS Tandem Solar Cells: From Certified 24.2% toward 30% and Beyond," *ACS Energy Lett.*, pp. 1298–1307, Mar. 2022, doi: 10.1021/acsenergylett.2c00274.

[22] M. A. Ruiz-Preciado *et al.*, "Monolithic Two-Terminal Perovskite/CIS Tandem Solar Cells with Efficiency Approaching 25%," *ACS Energy Lett.*, vol. 7, no. 7, pp. 2273–2281, Jul. 2022, doi: 10.1021/acsenergylett.2c00707.

[23] M. Nakamura, K. Yamaguchi, Y. Kimoto, Y. Yasaki, T. Kato, and H. Sugimoto, "Cd-Free Cu(In,Ga)(Se,S)2 Thin-Film Solar Cell With Record Efficiency of 23.35%," *IEEE J. Photovolt.*, vol. 9, no. 6, pp. 1863–1867, Nov. 2019, doi: 10.1109/JPHOTOV.2019.2937218.

[24] A. Corani *et al.*, "Ultrafast Dynamics of Hole Injection and Recombination in Organometal Halide Perovskite Using Nickel Oxide as p-Type Contact Electrode," *J. Phys. Chem. Lett.*, vol. 7, no. 7, pp. 1096–1101, Apr. 2016, doi: 10.1021/acs.jpclett.6b00238.

[25] D. Di Girolamo, F. Di Giacomo, F. Matteocci, A. G. Marrani, D. Dini, and A. Abate, "Progress, highlights and perspectives on NiO in perovskite photovoltaics," *Chem. Sci.*, vol. 11, no. 30, pp. 7746–7759, 2020, doi: 10.1039/D0SC02859B.

[26] N. Tiwari *et al.*, "Advances and Potentials of NiO x Surface Treatments for p−i−n Perovskite Solar Cells," *Sol. RRL*, vol. 6, no. 3, p. 2100700, 2022, doi: 10.1002/solr.202100700.

[27] C. C. Boyd *et al.*, "Overcoming Redox Reactions at Perovskite-Nickel Oxide Interfaces to Boost Voltages in Perovskite Solar Cells," *Joule*, vol. 4, no. 8, pp. 1759–1775, Aug. 2020, doi: 10.1016/j.joule.2020.06.004.

[28] N. Pant, A. Kulkarni, M. Yanagida, Y. Shirai, T. Miyasaka, and K. Miyano, "Investigating the Growth of CH3NH3PbI3 Thin Films on RF-Sputtered NiOx for Inverted Planar Perovskite Solar Cells: Effect of CH3NH3+ Halide Additives versus CH3NH3+ Halide Vapor Annealing," *Adv. Mater. Interfaces*, vol. 7, no. 3, p. 1901748, 2020, doi: 10.1002/admi.201901748.

[29] T. Kodalle, "Unraveling the structural and optoelectronic effects of Rb on Chalcopyrite solar cells," 2020, doi: 10.25673/33525.

[30] L. Gütay, D. Regesch, and J. K. Larsen, "Influence of copper excess on the absorber quality of CuInSe2," *Appl Phys Lett*, p. 4, 2011.

[31] R. Mainz *et al.*, "Sudden stress relaxation in compound semiconductor thin films triggered by secondary phase segregation," *Phys. Rev. B*, vol. 92, no. 15, p. 155310, Oct. 2015, doi: 10.1103/PhysRevB.92.155310.

[32] T. Rissom *et al.*, "Examination of growth kinetics of copper rich Cu(In,Ga)Se2-films using synchrotron energy dispersive X-ray diffractometry," *Sol. Energy Mater. Sol. Cells*, vol. 95, no. 1, pp. 250–253, Jan. 2011, doi: 10.1016/j.solmat.2010.05.007.

[33] T. Kodalle *et al.*, "Elucidating the Mechanism of an RbF Post Deposition Treatment in CIGS Thin Film Solar Cells," *Sol. RRL*, vol. 2, no. 9, p. 1800156, 2018, doi: 10.1002/solr.201800156.

[34] R. Ortega-Borges and D. Lincot, "Mechanism of Chemical Bath Deposition of Cadmium Sulfide Thin Films in the Ammonia-Thiourea System: In Situ Kinetic Study and Modelization," *J. Electrochem. Soc.*, vol. 140, no. 12, p. 3464, Dec. 1993, doi: 10.1149/1.2221111.

[35] M. Saliba *et al.*, "Cesium-containing triple cation perovskite solar cells: improved stability, reproducibility and high efficiency," *Energy Environ. Sci.*, vol. 9, no. 6, pp. 1989–1997, Jun. 2016, doi: 10.1039/C5EE03874J.

[36] A. Al-Ashouri, “Eliminating interface losses in Perovskite single junctions for efficient tandem solar cells,” 2021, doi: 10.14279/depositonce-12472.
[37] J. Bauer, O. Breitenstein, and J.-M. Wagner, “Lock-in Thermography: A Versatile Tool for Failure Analysis of Solar Cells,” p. 7.
[38] O. Breitenstein, “Illuminated versus dark lock-in thermography investigations of solar cells,” *Int. J. Nanoparticles*, vol. 6, no. 2–3, pp. 81–92, Jan. 2013, doi: 10.1504/IJNP.2013.054983.
[39] S.-G. Kim *et al.*, “How antisolvent miscibility affects perovskite film wrinkling and photovoltaic properties,” *Nat. Commun.*, vol. 12, no. 1, Art. no. 1, Mar. 2021, doi: 10.1038/s41467-021-21803-2.
[40] D. Greiner, S. E. Gledhill, Ch. Köble, J. Krammer, and R. Klenk, “Damp heat stability of Al-doped zinc oxide films on smooth and rough substrates,” *Thin Solid Films*, vol. 520, no. 4, pp. 1285–1290, Dec. 2011, doi: 10.1016/j.tsf.2011.04.190.
[41] V. M. Le Corre *et al.*, “Quantification of Efficiency Losses Due to Mobile Ions in Perovskite Solar Cells via Fast Hysteresis Measurements,” *Sol. RRL*, vol. 6, no. 4, p. 2100772, 2022, doi: 10.1002/solr.202100772.
[42] N. E. Courtier, J. M. Cave, J. M. Foster, A. B. Walker, and G. Richardson, “How transport layer properties affect perovskite solar cell performance: insights from a coupled charge transport/ion migration model,” *Energy Environ. Sci.*, vol. 12, no. 1, pp. 396–409, Jan. 2019, doi: 10.1039/C8EE01576G.
[43] I. Levine *et al.*, “Interface-Dependent Ion Migration/Accumulation Controls Hysteresis in MAPbI3 Solar Cells,” *J. Phys. Chem. C*, vol. 120, no. 30, pp. 16399–16411, Aug. 2016, doi: 10.1021/acs.jpcc.6b04233.
[44] W. Chen *et al.*, “Understanding the Doping Effect on NiO: Toward High-Performance Inverted Perovskite Solar Cells,” *Adv. Energy Mater.*, vol. 8, no. 19, p. 1703519, 2018, doi: 10.1002/aenm.201703519.
[45] Q. He, K. Yao, X. Wang, X. Xia, S. Leng, and F. Li, “Room-Temperature and Solution-Processable Cu-Doped Nickel Oxide Nanoparticles for Efficient Hole-Transport Layers of Flexible Large-Area Perovskite Solar Cells,” *ACS Appl. Mater. Interfaces*, vol. 9, no. 48, pp. 41887–41897, Dec. 2017, doi: 10.1021/acsami.7b13621.